AIAA JOURNAL
Vol. 49, No. 2, February 2011

Effects of Wall-Temperature Conditions on Effusion Cooling in a Supersonic Boundary Layer

Jens Linn[*] and Markus J. Kloker[†]
Institut für Aerodynamik und Gasdynamik, 70569 Stuttgart, Germany

DOI: 10.2514/1.J050383

The influence of effusion cooling through discrete holes on a laminar Mach 2.67 boundary layer is investigated using direct numerical simulation. It is found that the wall condition (isothermal, adiabatic, or radiative–adiabatic, with neglected heat conduction within the wall) has a very strong influence on the vortex systems that are generated by the holes and thus also on the cooling features. The transfer of results from short-duration isothermal shock-tunnel experiments to the more realistic radiative–adiabatic situation is difficult. In addition to trying to establish a coolant film at the wall, a significant increase of the wall shear should be avoided in order to not increase the heat flux into the wall.

Nomenclature

A = hole surface
Ma = Mach number
Re = Reynolds number
r_{eff} = effective hole radius
r_{mod} = modified hole radius
q = heat flux at the wall
T = temperature
$\bar{T}$ = spanwise mean temperature
u, v, w = velocity in x, y and z direction
x = downstream coordinate
y = wall-normal coordinate
z = spanwise coordinate
δ = boundary-layer thickness
ϵ = emission coefficient
η = cooling effectiveness
$\bar{\eta}$ = spanwise mean cooling effectiveness

Subscripts

ad = adiabatic
c = with cooling
$c1$ = values at the first row of holes
$c2$ = values at the second row of holes
is = isothermal
ra = radiative–adiabatic
ref = reference value (without cooling)
w = values at the wall
0 = stagnation conditions
∞ = freestream value

Superscript

$\star$ = dimensional value

I. Introduction

FOR reentry or hypersonic cruise vehicles the knowledge of the thermal loads and skin friction is of great importance for the design of the thermal protection system (TPS). For example, the space shuttle uses radiation cooling in combination with a material with very low thermal conductivity as TPS [1]. It is designed to withstand the hottest part of the flight trajectory and cannot be adjusted during the flight. These kinds of systems are called passive TPS. More recent studies focus on active TPS-like effusion and transpiration cooling. Here, the flow is directly affected so that the thermal loads are reduced. The strength of these systems is that they can adapt to the actual thermal load during the flight.

Effusion or film cooling is the state of the art for cooling turbine blades. Here, air is commonly used as the cooling gas and blown through holes or slits on the turbine blade surface into the flow. Goldstein [2] gives a comprehensive overview of previous studies concerning film cooling. Results of various experiments with air as cooling gas at low Mach numbers, 0.02 to 0.2, are summarized and compared with theoretical models. Many slot film-cooling investigations have been performed in the past, showing the relevant physical phenomena and important parameters [3–5].

Of greater practical interest for the cooling of turbine blades are investigations dealing with a single hole or with multiple rows of holes [6–9]. The influence of staggered and inline holes have been investigated by Jubran and Maiteh [7]. They found that a staggered hole configuration yields a much higher cooling effectiveness. In their experimental studies the holes were inclined at an angle of 35° with respect to the plate surface, and additionally inclined by 30° with respect to the plate surface as projected into the spanwise/normal plane. The best results were achieved in a staggered configuration, where the holes of the first row are simply inclined and those of the second row are inclined twice. All of these studies [6–9] have been performed in a turbulent subsonic boundary-layer flow, which is typical for turbine-blade cooling.

Most studies on effusion cooling in supersonic flows deal with a turbulent boundary layer in which a cold gas is injected by wall-normal blowing at the vehicle surface [10–13]. The ratio of specific cooling-gas mass flux to the corresponding freestream mass flux (the blowing ratio) is less than the ratio that is used for turbine-blade cooling, and the Mach numbers were between 2 and 3. The focus is on the cooling of scramjet combustion chambers or rocket chambers/nozzles. A steady axisymmetric Reynolds-averaged Navier–Stokes simulation of such a kind of effusion cooling of a rocket nozzle was done by Riccius et al. [14]. The walls of the nozzle in the sub- and transonic parts were modeled by a porous medium through which the coolant enters the nozzle. They additionally coupled a fluid solver with a heat transfer model to allow for a more realistic prediction for the effectiveness of the effusion cooling.

Received 10 December 2009; revision received 15 September 2010; accepted for publication 22 October 2010. Copyright © 2010 by Markus J. Kloker. Published by the American Institute of Aeronautics and Astronautics, Inc., with permission. Copies of this paper may be made for personal or internal use, on condition that the copier pay the $10.00 per-copy fee to the Copyright Clearance Center, Inc., 222 Rosewood Drive, Danvers, MA 01923; include the code 0001-1452/11 and $10.00 in correspondence with the CCC.

[*] Research Assistant, Aerospace Engineering Department, Pfaffenwaldring 21.

[†] Associate Professor, Aerospace Engineering Department, Pfaffenwaldring 21. Member AIAA.

The effusion cooling by blowing through slits and holes in the wall-normal direction into a laminar supersonic boundary layer has been the subject of more recent investigations [15–17]. In the experiments by Esser and Gülhan [15] no cooling effect was observed for blowing through discrete holes into a Mach 6 boundary layer. However, the reason most probably lies in a blowing rate that is too high. Heufer and Olivier [16,18,19] focus on an isothermal Mach 2.67 laminar boundary layer, which was effusion-cooled by spanwise slits and holes. A comparison of the slit configurations with numerical simulations by Linn and Kloker [17] indicates good agreement with the experimental data. In addition, two staggered rows of holes were investigated [16], and only a slightly lower cooling effectiveness was found, compared with the slit configuration.

The flow physics of effusion-hole configurations, aligned or staggered rows of holes, has also been analyzed for an adiabatic laminar Mach 6 boundary layer by Linn and Kloker [17,20]. It was found that aligned holes and a large spanwise spacing jeopardize laminarity of the flow. Nevertheless, no transition has been observed in these investigations, due to the weaker growth of the disturbance waves in supersonic flows as well as a weaker wall shear, compared with the incompressible case [20]. For this reason, staggered holes and a small spanwise spacing are preferable, which is also good for effusion cooling, because of the lower blowing velocities and a more homogeneous spanwise distribution.

The objective of this work is to investigate the influence of the wall-temperature condition, the blowing rate, and Reynolds number on the cooling of a Mach 2.67 laminar boundary layer. The flow parameters are taken from the work of Heufer and Olivier [16]. The paper is organized as follows: The numerical method, including the effusion modeling, is described in Sec. II, and Sec. III presents the results for isothermal and (radiation) adiabatic cases. Thermal conduction within the wall is neglected in this study.

II. Numerical Method

A. Governing Equation

The numerical method is based on the complete 3-D unsteady compressible Navier–Stokes equations, the continuity equation, and the energy equation:

$$\frac{\partial \rho}{\partial t} + \nabla \cdot (\rho \mathbf{u}) = 0 \tag{1}$$

$$\frac{\partial (\rho \mathbf{u})}{\partial t} + \nabla \cdot (\rho \mathbf{u}\mathbf{u}) + \nabla p = \frac{1}{Re} \cdot \nabla \boldsymbol{\sigma} \tag{2}$$

and

$$\frac{\partial (\rho e)}{\partial t} + \nabla \cdot (p + \rho e)\mathbf{u} = \frac{1}{(\kappa - 1) Re Pr Ma^2} \nabla \cdot (\vartheta \nabla T) + \frac{1}{Re} \nabla \cdot (\boldsymbol{\sigma} \mathbf{u}) \tag{3}$$

where

$$\boldsymbol{\sigma} = \mu((\nabla \mathbf{u} + \nabla \mathbf{u}^T) - \tfrac{2}{3}(\nabla \cdot \mathbf{u})\mathrm{I}) \tag{4}$$

is the viscous stress, and

$$e = c_v \cdot T + \tfrac{1}{2}(u^2 + v^2 + w^2) \tag{5}$$

is the total energy per mass unit. The air is considered as a nonreacting calorically perfect gas [21,22],

$$p = \frac{1}{\kappa Ma^2} \cdot \rho T \tag{6}$$

with a constant Prandtl number ($Pr = 0.71$) and specific heat ratio of $\kappa = c_p / c_v = 1.4$. The viscosity μ is calculated using Sutherland's law [23]. No bulk or second-viscosity ansatz has been used.

All length scales are dimensionless with respect to a reference length:

$$L^\star = \frac{\mu_\infty^\star \cdot Re}{\rho_\infty^\star \cdot u_\infty^\star} \tag{7}$$

Reference values for velocity, density temperature, viscosity, and conductivity are their freestream values at the inflow (indicated by subscript ∞). The pressure is normalized by $(\rho_\infty^\star u_\infty^{\star 2})$, where the superscript $\star$ denotes dimensional quantities. With these definitions, the global and running-length Reynolds numbers are, respectively, defined as

$$Re = \frac{\rho_\infty^\star \cdot u_\infty^\star \cdot L^\star}{\mu_\infty^\star} = 10^5 \quad \text{and} \quad Re_x = \frac{\rho_\infty^\star \cdot u_\infty^\star \cdot x^\star}{\mu_\infty^\star} = x \cdot Re \tag{8}$$

B. Discretization and Boundary Conditions

The Navier–Stokes equations are solved in a rectangular integration domain (Fig. 1) on the flat plate, which does not contain any shock wave induced by the leading edge. In the streamwise (x) and wall-normal (y) directions, discretization is realized by split compact finite differences of sixth order. In the spanwise (z) direction, the flow is assumed to be periodic; thus, a Fourier spectral approach is used for the z derivatives. Half of the integration domain in the spanwise direction is computed, since the flowfield is assumed to be symmetric. The time integration is done with the classical fourth-order Runge–Kutta method. A detailed description of the discretization and algorithm is reported in [24].

At the inflow boundary ($x = x_0$), profiles obtained from self-similarity solutions of boundary-layer theory are fixed for all variables. At the outflow ($x = x_N$), all equations are solved by neglecting the second x derivative terms ($\partial^2 / \partial x^2$). At the freestream boundary ($y = y_M$), the gradient of the flow variables is set to zero along spatial characteristics [21]. At the wall, all velocity components are zero, except at the hole surface. For the modeling of the holes, see Sec. II.C. The temperature outside the holes is either the local adiabatic-wall temperature, given by

$$\left. \frac{\partial T}{\partial y} \right|_w = 0 \tag{9}$$

or has a constant value (isothermal wall; $T_{w,\mathrm{is}} = \mathrm{const}$), or is the radiative–adiabatic-wall temperature, given by

$$\vartheta^\star \left. \frac{\partial T^\star}{\partial y^\star} \right|_w = \epsilon \sigma^\star T_w^{\star 4} \quad \text{with} \quad \epsilon = 0.8 \tag{10}$$

The pressure gradient in the wall-normal direction at the wall is set to zero ($\partial p / \partial y|_w = 0$).

C. Modeling of Blowing

The steady blowing of cold air through holes at the wall with a hole radius r_c is modeled by prescribing a wall-normal blowing-rate distribution:

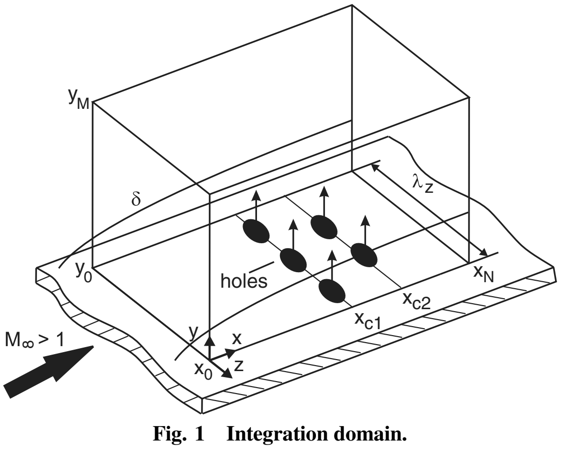

Fig. 1 Integration domain.

$$(\rho v)_c = (\rho v)_{c,\max} \cdot c(r) \qquad (11)$$

where $(\rho v)_{c,\max}$ is the maximum blowing rate at the hole center. The blowing-rate distribution over the hole is prescribed by a polynomial of fifth order $c(r)$ over the hole radius (see Fig. 2a). Both the gradient and curvature are zero at $r = 0$ and $r = r_c$:

$$c(r) = 1 - 6 \cdot \left(\frac{r}{r_c}\right)^5 + 15 \cdot \left(\frac{r}{r_c}\right)^4 - 10 \cdot \left(\frac{r}{r_c}\right)^3 \qquad (12)$$

with

$$r = \sqrt{(x - x_c)^2 + (z - z_c)^2}, \qquad 0 \le r \le r_c \qquad (13)$$

where x_c and z_c stand for the coordinates of the hole center. Outside the hole, (ρv) is zero at the wall. This kind of modeling has already been used for steady suction [25,26] and suction/blowing to introduce unsteady disturbances into the flow [27]. If not stated otherwise, blowing model B (see Fig. 2a) has been adopted.

The wall-temperature distribution over the holes is prescribed by

$$T_c = T_s \cdot (1 - c(r)) + T_{c,\text{core}} \cdot c(r) \qquad (14)$$

where $T_{c,\text{core}}$ is the core temperature of the cold air in the hole center, and T_s is the wall temperature at the hole edge (see Fig. 3a) on a ray running from the hole center through the considered grid point. For an isothermal wall, $T_s = T_w$. For an adiabatic or radiative–adiabatic wall, an iterative procedure is used, because the point S will mostly not coincide with a grid point. Typically, one or more grid points of the considered cell lie inside the hole (see Fig. 3). The temperature is at first unknown there and values of the previous iteration level are taken. The wall temperature in the case of a radiative–adiabatic wall with effusion cooling is shown in Sec. III.C. The modeling takes into account heat conduction between the effusing gas, and the hole edge smoothes sharp temperature gradients for T_c that are very different from T_s. Note that due to the low blowing velocity near the hole edge, the cooling-gas temperature in this region plays only a minor role.

III. Results

In the short-duration experiment at the shock wave laboratory at RWTH Aachen University, a laminar boundary layer on a wedge with a deflection angle of 30° and $T_w^\star = 293$ K has been investigated. The Mach number in front of the shock wave is $Ma_{\text{pre}} = 8.17$ and the total temperature $T_0^\star = 1390$ K [19]. Behind the shock the Mach number and temperature drop to $Ma_\infty = 2.67$ and $T_\infty^\star = 564$ K, respectively, which are our freestream conditions for all simulations. The postshock unit Reynolds number is $Re_{\text{unit}}^\star = 4.07 \times 10^6$ 1/m and the core temperature of the cooling gas, air, is the same in all simulations: $T_{c,\text{core}}^\star = T_w^\star = 293$ K ($T_w = 0.52$). For details of the experiment, see [16,19]. The hole parameters are summarized in Table 1.

The maximum blowing rate is $(\rho v)_{c,\max} = 0.21$ (model $\mathcal{B}$), and the corresponding average rate is $\overline{(\rho v)_c} = 0.105$. The investigated hole configuration consists of two staggered rows of holes (Fig. 2b), with an overlap of the holes in spanwise direction when looking downstream.

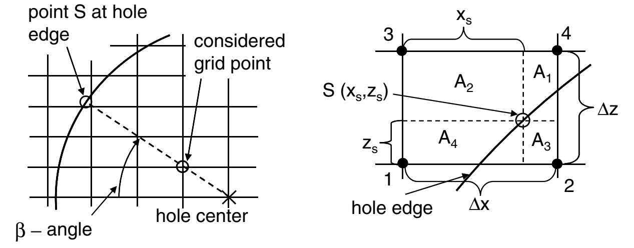

a) b)

Fig. 3 Sketches of a) hole on the grid at the wall and b) bilinear interpolation method for the wall temperature at the point *S*.

A. Comparison of Simulations with Blowing Pipe Included and Modeled Blowing

First, we compare our modeled blowing, model $\mathcal{B}$, with a simulation where we included the blowing pipe. Here, we look only at a single hole that has the same hole radius and cooling-gas temperature as prescribed above. In the simulation with a pipe we connect a rectangular domain with a cylindrical domain using bilinear interpolation. The pipe wall is isothermal, $T_w^\star = 293$ K. At the pipe inflow the pressure ($p_{\text{pi,inlet}} > p_\infty$) and temperature profiles are fixed and the v_{ax}-velocity modulus is variable, v_r and v_φ are set to zero, and v_{ax} is extrapolated from the internal pipe flowfield. The mass flux through the pipe follows the pressure difference between the pipe inlet and the pressure in the freestream. A Hagen–Poiseuille profile is used as initial condition for the pipe flow.

The streamwise position of the hole is $x_{c1} = 2.25$ and the blowing-rate and temperature distributions at the hole surface are shown for the two cases in Fig. 4. The maximum blowing rate and blowing mass flux is equal in both cases, but with modeled blowing the hole radius is slightly enlarged to yield an equal integral mass flux. In the case with a pipe, the maximum blowing rate is not in the hole center, in contrast to the modeled blowing. It lies downstream of the hole center near the hole edge. Near the upstream edge, gas from the boundary layer enters the pipe [$(\rho v)_{c,\min} = -0.017$ and $(\rho v)_{c,\max} = 0.205$]. Another difference is that the gradient $\partial v / \partial z$ is lower within the hole but is larger at the hole edge in the case with a pipe.

The vortical structures are illustrated in Fig. 5. In the case with a pipe, they are weaker and decay faster downstream. Hence, the spanwise deformation $\partial v / \partial z$ is smaller, but the structures, CVP and horseshoe vortex, are generally equal in both cases.

The temperature fields at $x = 2.3$ in Fig. 6 also show minor differences. The film-cooling effectiveness η_{is} [Eq. (15)] looks correspondingly (Fig. 7). In both cases stripes of low effectiveness develop, but in the case with modeled blowing these stripes have a lower value of η_{is}. The maximum value of η_{is} is the same in both

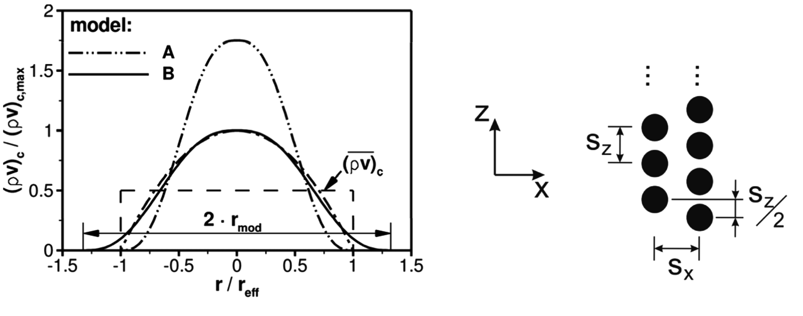

a) b)

Fig. 2 Sketches of a) numerical blowing models for a circular hole with radius r_{eff} and equal integral mass flow with identical radius and higher maximum blowing rate (dashed–double-dotted line); with radius $r_{\text{mod}} = 1.32 \cdot r_{\text{eff}}$ and equal maximum blowing rate (solid line); top-hat profile (dashed line); and Hagen–Poiseuille profile (dashed–single-dotted line) and b) hole configuration for the considered cases.

Table 1 Parameters of the hole configuration corresponding to Fig. 1 and parameters of the computational domain

Distance from the leading edge $x^\star_{c1}$, mm	$55\widehat{=}2.238$
Hole radius $r^\star_{\text{eff}}$, mm	$0.25\widehat{=}0.0102$
Modeled hole radius $r^\star_{\text{mod}}$	$0.331\widehat{=}0.01346$
Streamwise spacing $s^\star_x$, mm	$0.8\widehat{=}0.0326$
Spanwise spacing $s^\star_z$, mm	$0.8\widehat{=}0.0326$
Spanwise row offset, mm	$s^\star_z/2 = 0.4\widehat{=}0.0163$
Reference length $L^\star$, mm	24.57
Spanwise periodicity length	$\lambda_z = 0.8\widehat{=}0.0326$
Integration domain width	$0.4\widehat{=}0.0163$
Grid points $N_x \times M_y \times K_z$	$1802 \times 151 \times 33$
Step size in x Direction Δx	0.126×10^{-2}
Domain length $x_0 - x_N$	1.156–3.185
Step size in y direction $\Delta y_0 - \Delta y_M$	0.6×10^{-3}–2.048×10^{-3}
Domain height y_M	0.1629
Step size in z direction Δz	0.508×10^{-3}
Time step Δt	1.047×10^{-4}

cases. The case with modeled blowing thus underpredicts the spanwise averaged film-cooling effectiveness somewhat in the case with one hole row.

In conclusion, it can be said that the modeled blowing gives a lower bound of film-cooling effectiveness for one hole row if the maximum blowing rate and mass flux are equal meaning that the hole radius must be slightly increased with the employed modeling function ($r_{\text{mod}} > r_c$). For several-hole rows the reduced effectiveness may be weaker, due to interaction of vortices with the relatively low blowing rates investigated. In the following studies the modeled blowing is used.

B. Influence of the Wall-Temperature Condition

Here, we deal with three wall-temperature conditions: 1) isothermal, $T^\star_{w,\text{is}} = 293$ K; 2) adiabatic wall, without cooling $T^\star_{w,\text{ad}} \approx 1241.6$ K; and 3) radiative–adiabatic wall, without cooling $970 \geq T^\star_{w,\text{ra}} \geq 900$ K ($\epsilon = 0.8$). The wall temperature in the isothermal case is chosen as in the experimental case [16]. In this case the wall is strongly cooled, $T^\star_{w,\text{is}} \approx 0.41 \cdot T^\star_0$; thus, the wall has the temperature of the coolant gas. The streamwise velocity and temperature profiles for the three flows without cooling are shown in Figure 8.

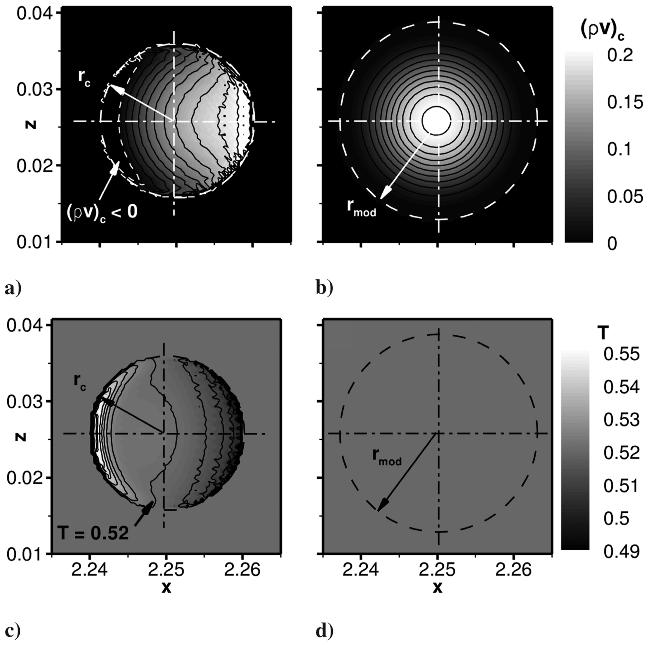

Fig. 4 Plots of $(\rho v)_c$ and T distribution at the wall: with blowing pipe (left) and with modeled blowing (right). For $(\rho v)_c$ isolines, $0.02 \leq (\rho v)_c \leq 0.2$ with $\Delta(\rho v)_c = 0.02$; dashed lines show $(\rho v)_c = 0$; and for T isolines, $0.49 \leq T \leq 0.54$ with $\Delta T = 0.005$. Note that $r_{\text{mod}} = 1.18 \cdot r_c$, and $(\rho v)_{c,\max,\text{mod}} > (\rho v)_{c,\max,\text{Hagen-Poiseuille}}$ at identical integral mass flux.

In Fig. 9 the vortex structures generated by the blowing through the holes are shown. Grossly seen, the adiabatic and radiative–adiabatic cases (Figs. 9b and 9c) look similar, and the isothermal case (Fig. 9a) differs strongly from the two other cases. But all cases have in common that each hole induces a counter-rotating vortex pair (CVP), with a rotation sense such that cool gas behind the holes is lifted up away from the wall. The CVPs from the first row are shifted in the wall-normal direction in the adiabatic and radiative–adiabatic cases. In the isothermal case they lie side by side, and the sonic line $Ma = 1$ exhibits a strong variation in spanwise direction. In the hole wake the flow is decelerated, and between the CVPs the flow is accelerated in the isothermal case. In the adiabatic and radiative–adiabatic cases the spanwise deformation of the sonic line is nearly zero. The reason lies in the different boundary-layer thicknesses δ for the different wall-temperature conditions. The ratio of the boundary-layer thickness of the isothermal to the adiabatic case is $\delta_{\text{is}}/\delta_{\text{ad}} = 0.68$ without cooling (see Fig. 8). The isothermal case has the strongest wall-normal gradient ($\partial u/\partial y|_w$), causing only a small deflection of the streamlines, in contrast to the adiabatic cases. This parameter has a very strong influence on the downstream evolution of the vortices; if $\partial u/\partial y|_w$ is large, an overlapping of the vortices does not occur, and the vortices only decay slowly downstream. A faster homogenization takes place in the adiabatic and radiative–adiabatic cases, due to the lower streamwise velocity in the near-wall region.

C. Influence of the Blowing Rate

The blowing rate $(\rho v)_{c,\max}$ has been varied to investigate its influence on the effusion-cooling effectiveness. The isothermal effusion-cooling effectiveness is defined by

$$\eta_{\text{is}} = 1 - \frac{\dot{q}_c}{\dot{q}_{\text{ref}}} \tag{15}$$

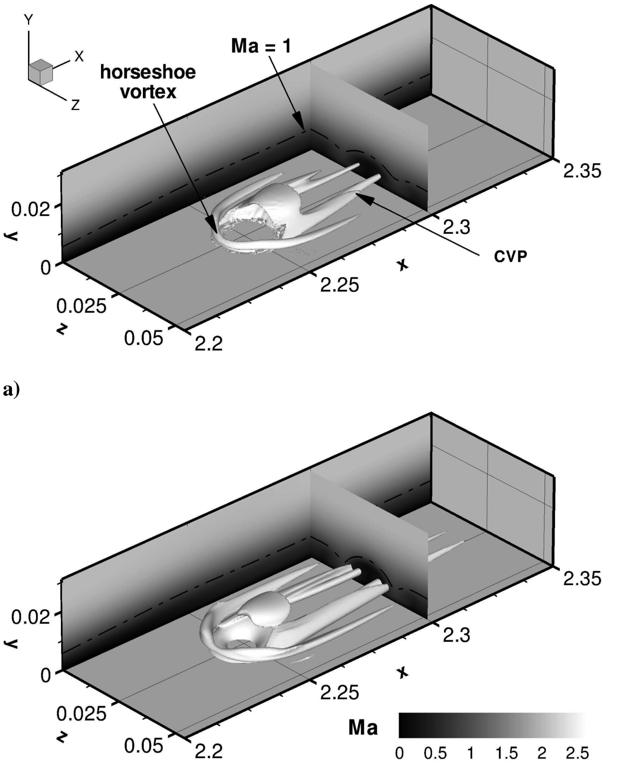

Fig. 5 Visualization of the vortical structures via λ_2 isosurface ($\lambda_2 = -60$) for the cases a) with blowing pipe and b) with modeled blowing.

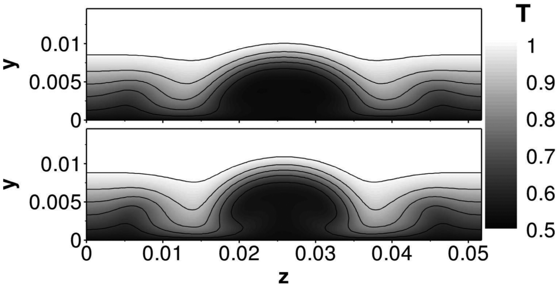

Fig. 6 Crosscuts of the temperature field at $x = 2.3$ for the simulation with blowing pipe (top) and modeled blowing (bottom); for T isolines, $0.5 \leq T \leq 1$ with $\Delta T = 0.1$.

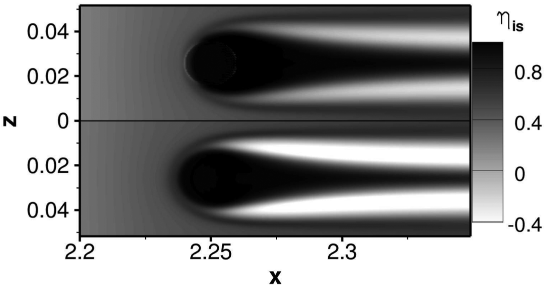

Fig. 7 Cooling effectiveness η_{is} for the isothermal-wall case with blowing pipe (top) and modeled blowing (bottom).

where $\dot{q}_{ref}$ is the reference heat flux at the wall without effusion cooling, and $\dot{q}_c$ is the heat flux with effusion cooling (see also [16,19]). Figure 10 displays the effusion-cooling effectiveness for the three blowing rates $(\rho v)_{c,\max} = 0.105$, 0.15, and 0.21. For all rates streamwise streaks develop behind the holes. Negative values mean that the heat flux into the wall is larger than without blowing, and these regions get larger with increasing blowing rate. In the accelerated areas, the wall shear is increased and, additionally, hot gas from the freestream is transported to the wall; thus, the heat flux increases. Directly behind the holes, in the decelerated areas with lowered wall shear, cold gas from the wall (that keeps constantly cool) is transported away from the wall. With increasing blowing rate the cooling effectiveness decreases, because the vortices get stronger and the regions with increased wall shear enlarge. In addition, the cold gas is blown further up into the boundary layer. In front of the first row the effusion-cooling effectiveness increases with increasing blowing rate. This happens because of increasing blockage, causing flow deceleration with decreasing wall shear.

The cooling effectiveness for different blowing rates downstream of the holes is shown in Fig. 11 and compared with experimental data from [16]. The spanwise position of the measured points in the experiment is unknown; therefore, the spanwise mean, minimum, and maximum cooling effectiveness levels from the simulation are plotted. The spanwise mean fits the experimental data well; the simulation only predicts a slightly higher cooling effectiveness. We note that using blowing model A (see Fig. 2) results in a too-early reduction of η_{is} for $\overline{\rho v}_c \geq 0.05$, which is a consequence of the high $(\rho v)_{c,\max}$.

A validation of the grid resolution for the isothermal case with a blowing rate $(\rho v)_{c,\max} = 0.21$ is shown in Fig. 12. The spatial spacings in the x, y, and z directions are halved, in contrast to the case with the standard grid (see Table 1). The u, v, and T profiles at three diameters behind the holes show a very good agreement at the two z

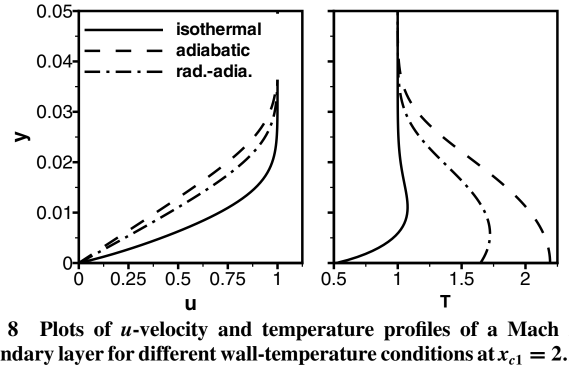

Fig. 8 Plots of u-velocity and temperature profiles of a Mach 2.67 boundary layer for different wall-temperature conditions at $x_{c1} = 2.238$.

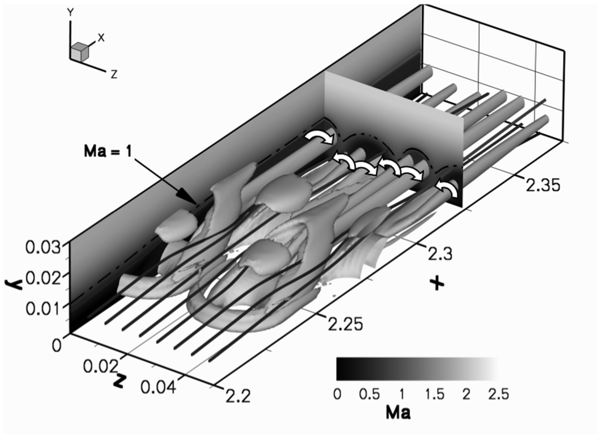

a) Isothermal wall

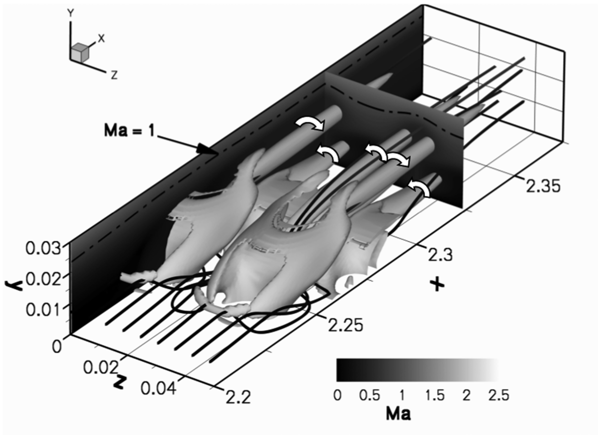

b) Adiabatic wall

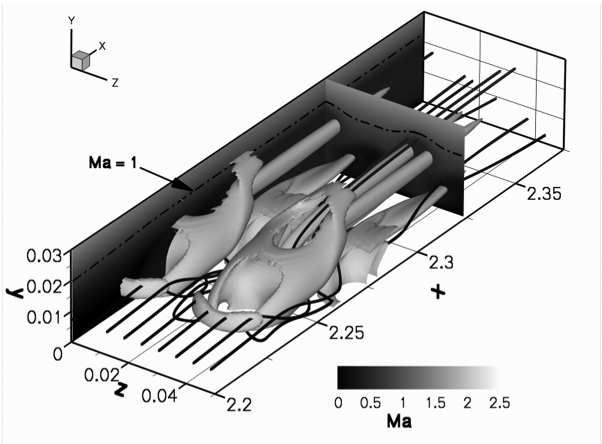

c) Radiative-adiabatic wall

Fig. 9 Visualization of vortex structures via λ_2 criterion [28] and streamlines for two staggered row of holes with different wall boundary conditions ($\lambda_2 = -30$). Longitudinal and crosscut of the local Mach number field with the sonic line (dashed lines denotes $Ma = 1$).

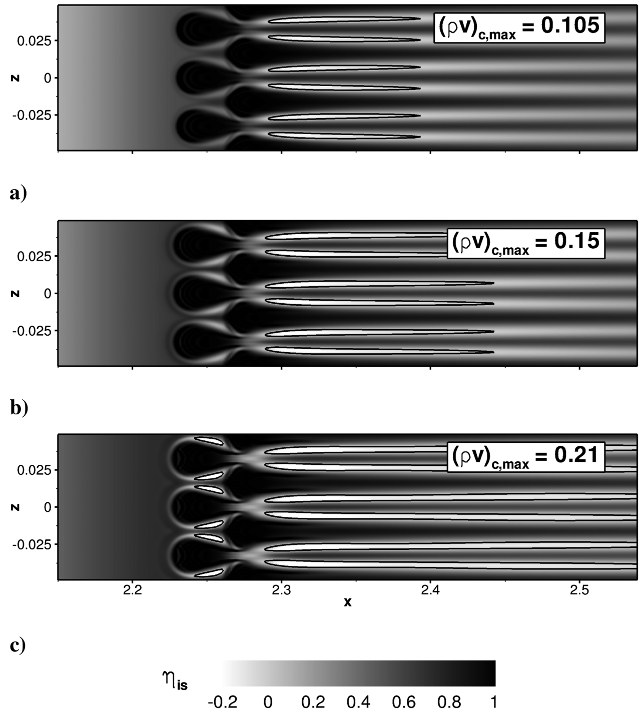

Fig. 10 Cooling effectiveness η_{is} for the isothermal-wall case with various blowing rates [$(\rho v)_{c,\max} = 0.105$, 0.15, and 0.21] and with two staggered rows of holes. Solid lines denote the isoline of the effusion-cooling effectiveness for $\eta_{\mathrm{is}} = 0.0$.

positions. At $z = 0.016$, the v profile shows only slight differences near the wall, but the overall agreement is very good.

For the adiabatic-wall condition the definition of the isothermal effusion-cooling effectiveness η_{is} is not valid anymore, because the heat flux $\dot{q}$ is zero by definition, but the wall temperature varies. Thus, we use the adiabatic effusion-cooling effectiveness η_{ad}, defined by

$$\eta_{\mathrm{ad}} = \frac{T^{\star}_{w,\mathrm{ad}} - T^{\star}_{w,c}}{T^{\star}_{w,\mathrm{ad}} - T^{\star}_{c,\mathrm{core}}} \tag{16}$$

with the adiabatic-wall temperature $T^{\star}_{w,\mathrm{ad}}$, the cooling-gas core temperature $T^{\star}_{c,\mathrm{core}}$, and the actual local wall temperature with effusion cooling $T^{\star}_{w,c}$. If the local wall temperature is equal to $T^{\star}_{c,\mathrm{core}}$ the cooling effectiveness is one.

Figure 13 shows the η_{ad} distribution. In contrast to the isothermal case, η_{ad} decreases here in the near wake of the holes with increasing blowing rate, but further downstream it increases. The reason is that at low blowing the coolant gas keeps closer to the wall, but further downstream the amount blown in dominates. More (cool) gas is injected with higher blowing rate, the boundary layer gets thicker, and thus the wall shear decreases. (We note that with an extremely cool gas, a low blowing rate, and large perforation area the boundary layer may get thinner despite mass injection. But this is not the case here.) The cooling effectiveness is nearly uniform in the spanwise direction behind the holes, in contrast to the isothermal case.

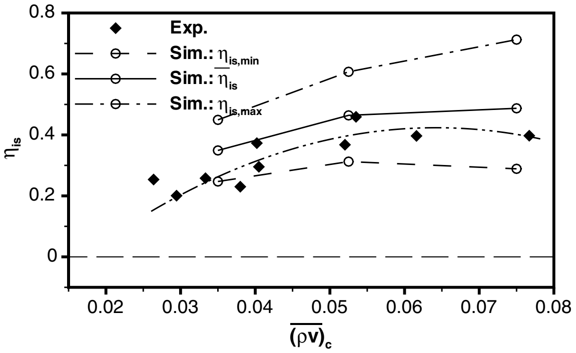

Fig. 11 Comparison of the cooling effectiveness η_{is} from experiment [16] and simulation for different blowing rates $\overline{(\rho v)}_c$ at $x = 2.645$.

In the radiative–adiabatic case Eq. (16) is also applied, but here we use the radiative–adiabatic-wall temperature:

$$\eta_{\mathrm{ra}} = \frac{T^{\star}_{w,\mathrm{ra}} - T^{\star}_{w,c}}{T^{\star}_{w,\mathrm{ra}} - T^{\star}_{c,\mathrm{core}}} \tag{17}$$

The behavior of the radiative–adiabatic wall for the different blowing rates is roughly similar (see Fig. 14), but the inclusion of isothermal features, albeit weakly, causes a somewhat weaker homogenization. Again, with increasing blowing rate the effectiveness is decreased directly behind the holes, but further downstream the cooling effectiveness is increased with increasing blowing rate. The wall-temperature distribution arising from the blowing is illustrated in Fig. 15 for the radiative–adiabatic case with a blowing rate $(\rho v)_{c,\max} = 0.21$.

The spanwise mean of the cooling effectiveness $\bar{\eta}$ for the different cases is illustrated in Fig. 16. The x coordinate is mapped on to ξ such that the coordinate origin is at the position of the second row x_{c2} and is related to $\overline{(\rho v)}_c \cdot A$, where $A = \pi \cdot r^2_{\mathrm{eff}}$ is the hole surface. This scaling enables a better conclusion of how efficiently the coolant gas is introduced into the boundary layer.

For the isothermal case the cooling effectiveness drops directly behind the holes, but slightly increases further downstream up to a maximum, followed by monotonic decay. Higher rates cause larger drops but higher maxima downstream. The increase of the cooling effectiveness corresponds with vanishing negative η_{is} in Fig. 10. With higher blowing rates the cooling effectiveness for the adiabatic and radiative–adiabatic cases increases directly behind the holes, but further downstream all three curves merge. The radiative–adiabatic case exhibits a higher effectiveness directly behind the holes, but further downstream it is lower than in the adiabatic case: With effusion cooling, the radiated heat decreases, and this difference is lost. The wall temperature is much lower anyway, of course.

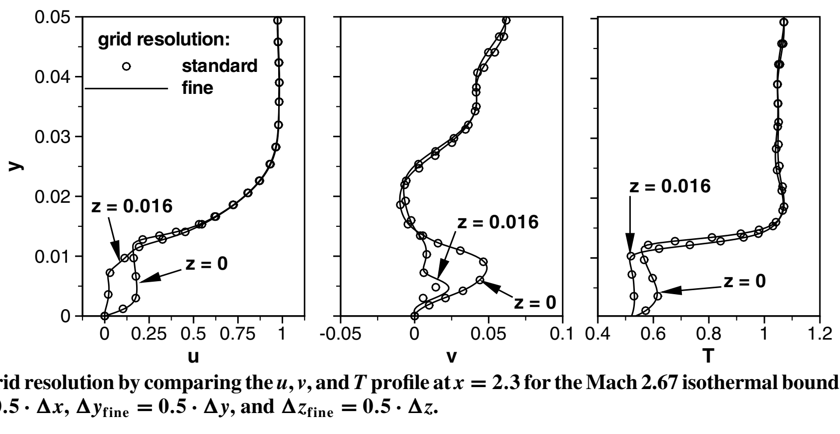

Fig. 12 Validation of the grid resolution by comparing the u, v, and T profile at $x = 2.3$ for the Mach 2.67 isothermal boundary layer with a blowing rate $(\rho v)_{c,\max} = 0.21$; $\Delta x_{\mathrm{fine}} = 0.5 \cdot \Delta x$, $\Delta y_{\mathrm{fine}} = 0.5 \cdot \Delta y$, and $\Delta z_{\mathrm{fine}} = 0.5 \cdot \Delta z$.

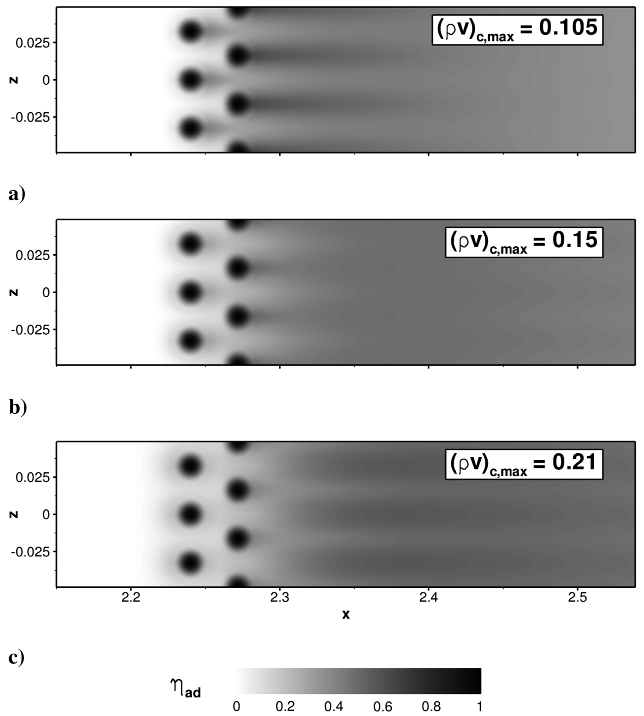

Fig. 13 Cooling effectiveness η_{ad} for the adiabatic-wall case with different blowing rates and with two staggered rows of holes.

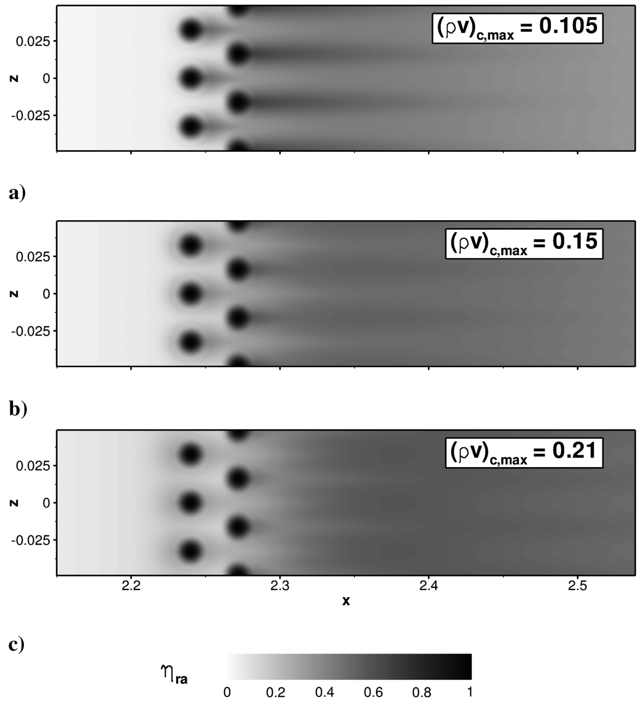

Fig. 14 Cooling effectiveness η_{ra} for the radiative–adiabatic-wall case with different blowing rates and with two staggered rows of holes.

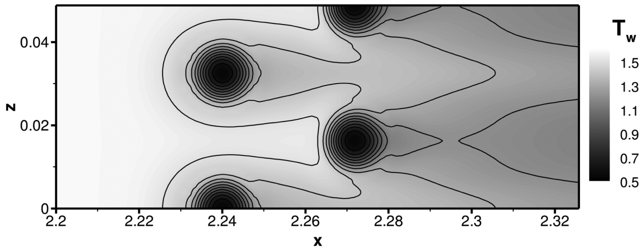

Fig. 15 Distribution of the wall temperature T_w for the Mach 2.67 radiative–adiabatic boundary layer with blowing rate $(\rho v)_{c,max} = 0.21$ (for T isolines, $0.6 \leq T \leq 1.7$ with $\Delta T = 0.1$).

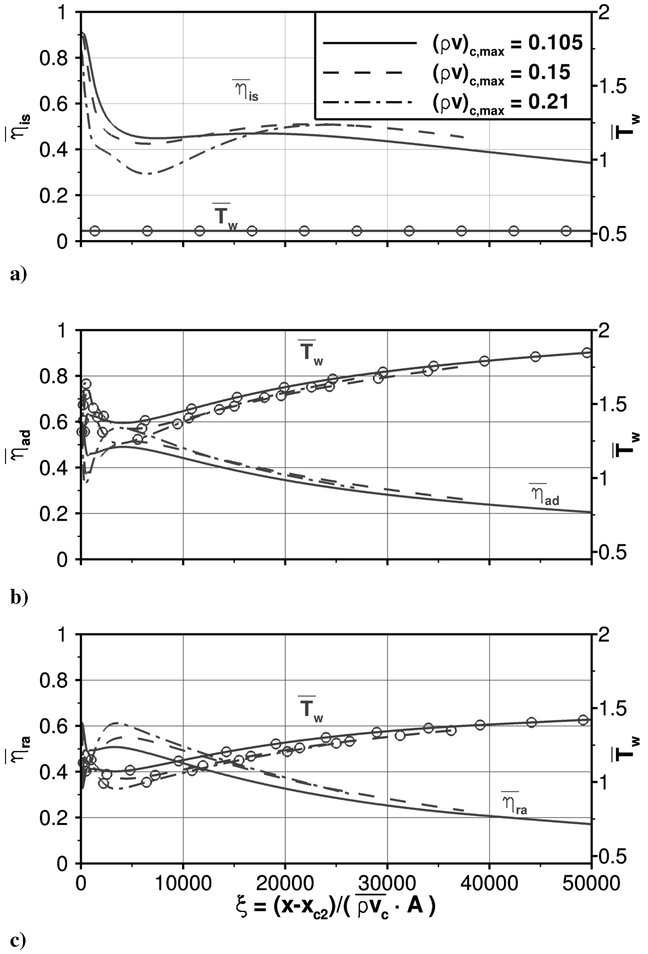

Fig. 16 Spanwise mean cooling effectiveness $\bar{\eta}_{is}$, $\bar{\eta}_{ad}$, and $\bar{\eta}_{ra}$ of a laminar Mach 2.67 flat-plate boundary layer for different blowing rates and wall conditions: a) isothermal, b) adiabatic, and c) radiative–adiabatic; $\xi = 10,000$, $(\rho v)_{c,max} = 0.105 \Rightarrow x \approx 2.6$, $(\rho v)_{c,max} = 0.15 \Rightarrow x \approx 2.75$, and $(\rho v)_{c,max} = 0.21 \Rightarrow x \approx 2.94$.

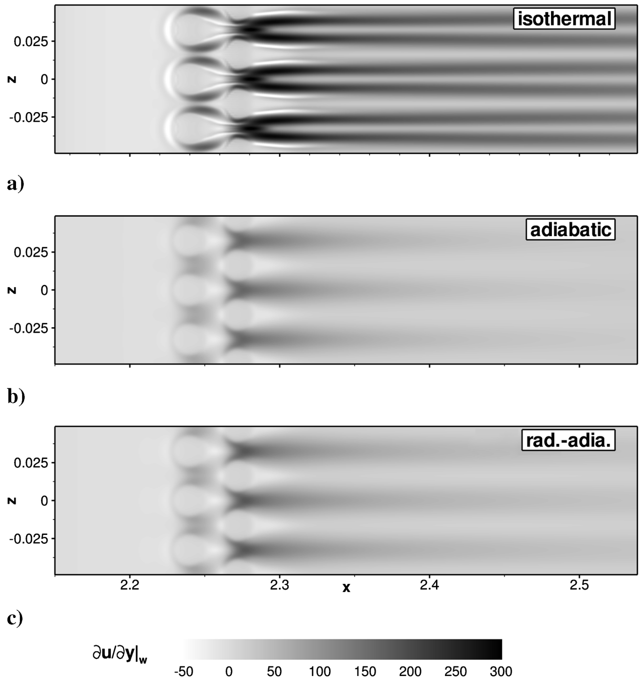

Fig. 17 $\partial u/\partial y|_w$ at the wall for the blowing rate $(\rho v)_{c,max} = 0.21$ in the isothermal, adiabatic, and radiative–adiabatic-wall cases, respectively.

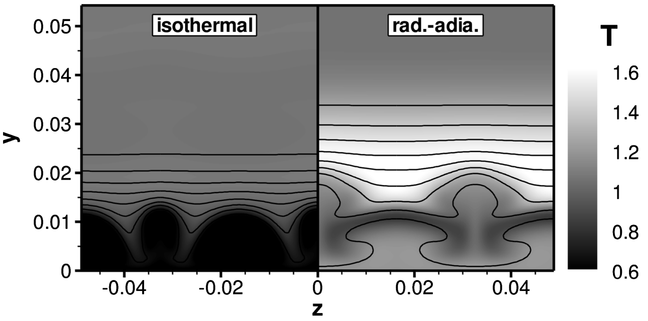

Fig. 18 Crosscut of the temperature flowfield with u isolines at $x = 2.3$ for the isothermal and adiabatic-wall cases with $(\rho v)_{c,\max} = 0.21$ (for u isolines, $0.1 < u < 0.9$ with $\Delta u = 0.1$).

The regions with high cooling effectiveness correspond to regions where $\partial u/\partial y|_w$ is low (see Fig. 17). Here, the gradients for the isothermal and radiative–adiabatic cases are shown for the highest blowing rate. For the isothermal case the black regions correspond to the white low-η_{is} regions in Fig. 10. At the side of the holes and in the downwash regions of the vortices, η_{is} is low and the wall shear is large. This clearly indicates the influence of the flow on the cooling effectiveness, in addition to a coolant layer (film). In the radiative–adiabatic case the gradient is much lower, but the same holds.

Crosscuts of the temperature fields for the isothermal and radiative–adiabatic cases are displayed in Fig. 18. (The radiative–adiabatic and adiabatic cases look very similar.) In the radiative–adiabatic case, a layer of cold gas is at the wall. In the isothermal case a continuous cold film does not exist. The CVPs caused by the blowing provide transport of cold gas from the wall into the boundary layer only locally.

D. Influence of the Reynolds Number

For the radiative–adiabatic case with a blowing rate $(\rho v)_{c,\max} = 0.21$ from Sec. III.B, the influence of the Reynolds number $Re_{x,c1} = x_{c1} \cdot Re$ is investigated by shifting the position of the row of holes downstream. Mass flux, hole configuration, and cooling-gas temperature were kept. The results are illustrated in Fig. 19. By increasing $Re_{x,c1}$ the cooling effectiveness decreases. The same holds for the wall temperature. Note that $\partial u/\partial y|_w$ gets smaller because the boundary layer grows, and thus the coolant gas does not stay as close to the wall. The decrease of $\partial u/\partial y|_w$ is not as strong in the radiative–adiabatic case as in the adiabatic or isothermal cases, because the boundary-layer growth is slightly less than proportional to $\sqrt{x}$, which is a consequence of the decreasing wall temperature and thus higher density.

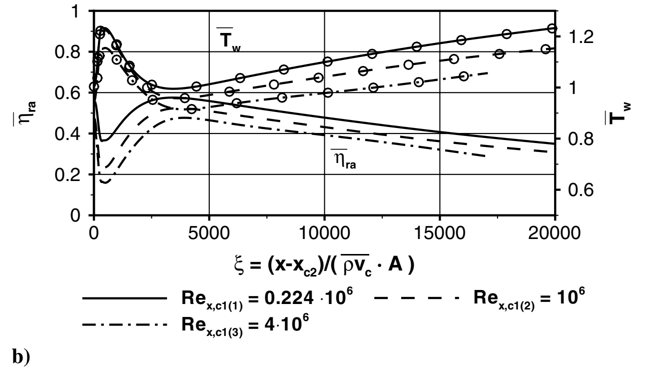
a)

b)

Fig. 19 Plots of a) downstream base flow temperature evolution and b) spanwise mean cooling effectiveness $\bar{\eta}_{\mathrm{ra}}$ of a laminar Mach 2.67 radiative–adiabatic flat-plate boundary layer for three local Reynolds numbers ($Re_{x,c1(1)} = 0.224 \times 10^6$, $Re_{x,c1(2)} = 10^6$, and $Re_{x,c1(3)} = 4 \times 10^6$; $(\rho v)_{c,\max} = 0.21$) at the blowing position.

IV. Conclusions

Simulations of effusion-cooled zero-pressure-gradient laminar boundary layers by discrete staggered holes have been performed using modeled blowing. A comparison of the cooling effectiveness with experimental data for an isothermal Mach 2.67 laminar boundary layer shows very good agreement in the case of a blowing model, with a maximum blowing rate corresponding to the maximum rate of an assumed Hagen–Poiseuille velocity profile. The modeling of blowing is not a major source of uncertainty for a coolant flow with zero axial vorticity, because simulations including the blowing pipe for one hole row showed only minor differences for the used blowing rates. Employing the modeling, the vortices downstream of the blowing are slightly, but not significantly, stronger.

A comparison of the wall-temperature conditions (isothermal, adiabatic, and radiative–adiabatic) shows a large impact on the flowfield and on the effusion-cooling effectiveness. The cases with adiabatic and radiative–adiabatic walls show grossly similar behavior, referring to the vortex structures and film-cooling effectiveness. The case with the isothermal cool wall represents a case at shock-tunnel conditions, indicating a different behavior. The vortex structures are much stronger, and regions at the wall exist where the heat loads are distinctly higher than in the case without cooling. Thus, short-duration experiments in shock tunnels cannot be simply transferred to cases with radiative–adiabatic wall because of the different states of the wall. The wall shear has a strong influence on the cooling effectiveness. First, a large $\partial u/\partial y|_w$ of the uncooled base flow keeps the coolant gas closer to the wall and is beneficial in this respect. Second, in the regions with a lowered $\partial u/\partial y|_w$ the cooling effectiveness is high, in contrast to regions with increased values of $\partial u/\partial y|_w$. Increasing the Reynolds number by shifting the hole position downstream translates into a decrease in the cooling effectiveness, because $\partial u/\partial y|_w$ of the base flow decreases.

Generally, the heat load depends on the Stanton number, which is related to the wall shear and the difference between the recovery temperature and the actual wall temperature. Film cooling means that a film of coolant gas lies at the wall, reducing both the temperature difference and the mean wall shear (by lowering the viscosity), and can best be realized by spanwise slits. For effusion cooling through holes the alteration of the local wall shear is of more importance, due to the induced vortex structures. Regions of enhanced wall shear exist, increasing locally the heat load at the hole sides and at high-velocity streaks downstream of the hole sides. The effect is most pronounced for a very cool wall, but is much weaker for a radiative–adiabatic wall. For the investigated blowing rates up to 21%, no self-induced unsteadiness could be observed; the wall shear is lower than for incompressible flow. Nevertheless, slits or a large number of microholes with a low blowing rate seem preferable.

Acknowledgments

Financial support has been provided by the German Research Council [Deutsche Forschungsgemeinschaft (DFG)] in the framework of the Special Research Center SFB-TRR 40. Computational resources have been kindly provided by the Stuttgart High-Performance Computing Center (HLRS).

References

[1] Curry, D. M., “Space Shuttle Orbiter Thermal Protection System Design and Flight Experience,” NASA TM-104773, 1993.

[2] Goldstein, R. J., “Film Cooling,” *Advances in Heat Transfer*, edited by T. F. Irvine, and J. P. Hartnett, Vol. 7, Academic Press, New York, 1971, pp. 321–379.

[3] Taslim, M. E., and Spring, S. D., “Experimental Investigations of Film Cooling Effectiveness for Slots of Various Exit Geometries,” *Journal of Thermophysics and Heat Transfer*, Vol. 6, No. 2, 1992, pp. 302–307. doi:10.2514/3.359

[4] Fitt, A. D., Ockendon, J. R., and Jones, T. V., “Aerodynamics of Slot Film Cooling: Theory and Experiment,” *Journal of Fluid Mechanics*, Vol. 160, 1985, pp. 15–27. doi:10.1017/S0022112085003366

[5] Fitt, A. D., and Wilmot, P., “Slot Film Cooling—The Effect of Separation Angle,” *Acta Mechanica*, Vol. 103, 1994, pp. 79–88. doi:10.1007/BF01180219

[6] Goldstein, R. J., and Jin, P., “Film Cooling Downstream of a Row of Discrete Holes with Compound Angle,” *Proceedings of the International Gas Turbine and Aeroengine Congress and Exhibition*, Vol. 123, 2001, pp. 222–230.

[7] Jubran, B. A., and Maiteh, B. Y., “Film Cooling and Heat Transfer from a Combination of Two Rows of Simple and/or Compound Angle Holes in Inline and/or Staggered Configuration,” *Heat and Mass Transfer*, Vol. 34, 1999, pp. 495–502. doi:10.1007/s002310050287

[8] Maiteh, B. Y., and Jubran, B. A., “Effects of Pressure Gradient on Film Cooling Effectiveness from Two Rows of Simple and Compound Angle Holes in Combination,” *Energy Conversion and Management*, Vol. 45, 2004, pp. 1457–1469. doi:10.1016/j.enconman.2003.09.007

[9] Saumweber, C., and Schulz, A., “Interaction of Film Cooling Rows: Effects of Hole Geometry and Row Spacing on the Cooling Performance Downstream of the Second Row of Holes,” *Journal of Turbomachinery*, Vol. 126, 2004, pp. 237–246. doi:10.1115/1.1731395

[10] Aupoix, B., Mignosi, A., Viala, S., Bouvier, F., and Gaillard, R., “Experimental and Numerical Study of Supersonic Film Cooling,” *AIAA Journal*, Vol. 36, No. 6, 1998, pp. 915–923. doi:10.2514/2.495

[11] Bass, R., Hardin, L., Rodgers, R., and Ernst, R., “Supersonic Film Cooling,” AIAA Paper 90-5239, 1990.

[12] Juhany, K. A., and Hunt, M. L., “Flowfield Measurements in Supersonic Film Cooling Including the Effect of Shock-Wave Interaction,” *AIAA Journal*, Vol. 32, No. 3, 1994, pp. 578–584. doi:10.2514/3.12024

[13] Juhany, K. A., Hunt, M. L., and Sivo, J. M., “Influence of Injection Mach Number and Temperature on Supersonic Film Cooling,” *Journal of Thermophysics and Heat Transfer*, Vol. 8, No. 1, 1994, pp. 59–65. doi:10.2514/3.501

[14] Riccius, J. R., Greuel, D., Haidn, O. J., and Leicht, T., “Coupled CFD Analysis of the Hot Gas and the Coolant Flow in Effusion Cooled Combustion Chambers,” AIAA Paper 2005-4437, 2005.

[15] Esser, B., and Gülhan, A., “Qualification of Active Cooling Concepts in Ground Facilities,” *RESPACE—Key Technologies for Reusable Space Systems, Notes on Numerical Fluid Mechanics and Multidisciplinary Design*, Vol. 98, edited by A. Gülhan, Springer, New York, 2008, pp. 104–131.

[16] Heufer, K. A., and Olivier, H., “Experimental Study of Active Cooling in 8 Laminar Hypersonic Flows,” *RESPACE - Key Technologies for Reusable Space Systems, Notes on Numerical Fluid Mechanics and Multidisciplinary Design*, edited by A. Gülhan, Vol. 98, Springer, New York, 2008, pp. 132–150.

[17] Linn, J., and Kloker, M. J., “Numerical Investigations of Film Cooling,” *RESPACE—Key Technologies for Reusable Space Systems, Notes on Numerical Fluid Mechanics and Multidisciplinary Design*, Vol. 98, edited by A. Gülhan, Springer, New York, 2008, pp. 151–169.

[18] Heufer, K. A., and Olivier, H., “Experimental and Numerical Study of Cooling Gas Injection in Laminar Supersonic Flow,” *AIAA Journal*, Vol. 46, No. 11, 2008, pp. 2741–2751. doi:10.2514/1.34218

[19] Heufer, K. A., and Olivier, H., “Film Cooling for Hypersonic Flow Conditions,” *Proceedings of the 5th European Workshop on Thermal Protection Systems and Hot Structures*, 2006.

[20] Linn, J., and Kloker, M. J., “Direct Numerical Simulation of Film Cooling in Hypersonic Boundary-Layer Flow,” *High Performance Computing in Science and Engineering ’08*, Springer, New York, 2009, pp. 171–189.

[21] Eißler, W., “Numerische Untersuchungen zum Laminar-%urbulenten Strömungsmschlag in Überschallgrenzschichten,” Ph.D. Thesis, Universität Stuttgart, Stuttgart, Germany, 1995.

[22] Thumm, A., “Numerische Untersuchung zum Laminar-Turbulenten Strömungsumschlag in Transsonischen Grenzschichtströmungen,” Ph. D. Thesis, Universität Stuttgart, Stuttgart, Germany, 1991.

[23] White, F. M., *Viscous Fluid Flow*, McGraw–Hill, New York, 1991.

[24] Babucke, A., Linn, J., Kloker, M. J., and Rist, U., “Direct Numerical Simulation of Shear-Flow Phenomena on Parallel Vector Computers,” *High Performance Computing on Vector Systems*, Springer, New York, 2003, pp. 229–247.

[25] Messing, R., and Kloker, M. J., “DNS Study of Spatial Discrete Suction for Laminar Flow Control,” *High Performance Computing in Science and Engineering ’04*, edited by E. Krause, and W. Jäeger, Springer, Berlin, 2005, pp. 163–175.

[26] Messing, R., and Kloker, M. J., “Investigation of Suction for Laminar Flow Control of Three-Dimensional Boundary Layers,” *Journal of Fluid Mechanics*, Vol. 658, 2010, pp. 117–147. doi:10.1017/S0022112010001576

[27] Stemmer, C., “Direct Numerical Simulation of Harmonic Point Source Disturbances in an Airfoil Boundary Layer with Adverse Pressure Gradient,” Ph.D. Thesis, Universität Stuttgart, Stuttgart, Germany, 2001.

[28] Jeong, J., and Hussain, F., “On the Identification of a Vortex,” *Journal of Fluid Mechanics*, Vol. 285, 1995, pp. 69–94. doi:10.1017/S0022112095000462

N. Chokani
Associate Editor